行政院國家科學委員會專題研究計畫　成果報告

利用化學控制合成新穎電子/離子作用氧化物及其特性分析

(3/3)

計畫類別：個別型計畫
計畫編號：NSC93-2113-M-002-006-
執行期間：93 年 08 月 01 日至 94 年 07 月 31 日
執行單位：國立臺灣大學化學系暨研究所

計畫主持人：劉如熹

計畫參與人員：陳浩銘、康佳正、郭慧通、陳錦昌、林益山、黃妃婷、賴泓均、劉宇桓、彭歆傑、黃文彥、梁雅麗

報告類型：完整報告
報告附件：出席國際會議研究心得報告及發表論文
處理方式：本計畫可公開查詢

中　華　民　國 94 年 10 月 24 日

行政院國家科學委員會補助專題研究計畫成果報告

利用化學控制合成新穎電子/離子作用氧化物及其特性分析(3/3)

計畫類別：■ 個別型計畫　□ 整合型計畫

計畫編號：NSC 93-2113-M-002-006

執行期間：93 年 8 月 1 日至 94 年 7 月 31 日

計畫主持人：劉如熹

共同主持人：

計畫參與人員：陳浩銘、康佳正、郭慧通、陳錦昌、林益山、黃妃婷
賴泓均、劉宇桓、彭歆傑、黃文彥、梁雅麗

成果報告類型(依經費核定清單規定繳交)：□精簡報告　■完整報告

本成果報告包括以下應繳交之附件：

□赴國外出差或研習心得報告一份

□赴大陸地區出差或研習心得報告一份

■出席國際學術會議心得報告及發表之論文各一份

□國際合作研究計畫國外研究報告書一份

處理方式：除產學合作研究計畫、提升產業技術及人才培育研究計畫、列管計畫及下列情形者外，得立即公開查詢

□涉及專利或其他智慧財產權，□一年□二年後可公開查詢

執行單位：台灣大學化學系

中　華　民　國　94　年　10　月　12　日

行政院國家科學委員會專題研究計畫成果報告
利用化學控制合成新穎電子/離子作用氧化物及其特性分析(3/3)
Synthesis by Chemical Control and Characterization of New Electronic/Ionic Oxides

計畫編號：NSC 93-2113-M-002-006
執行期限：93 年 8 月 1 日至 94 年 7 月 31 日
主持人：劉如熹 教授（台灣大學化學系）

一、中文摘要

隨科技之進步，資訊產業之發展也日新月異，資訊產品愈來愈多樣化，且持續有各式各樣之紀錄媒體相繼研發中，藉以滿足人類對大量資料儲存與紀錄上之需求。自 1995 年具穿隧式磁電阻(tunneling magnetoresistance; TMR)效應之材料得到突破性之進展，短短幾年內，其磁性感應度即提高一倍以上。TMR 於室溫時之 25~50 % 磁電阻值，遠遠高於傳統之巨磁電阻(giant magnetoresistance; GMR)材料(室溫~ 10 %)，使其對於各式紀錄媒體而言更具發展潛力。有鑑於此，本研究於第一部分，乃藉由化學取代將離子半徑較小之鈣離子取代離子半徑較大之鍶離子，合成具 TMR 效應$(Sr_{2-x}Ca_x)FeMoO_6$ $(0 \le x \le 2.0)$之系統，藉以探討化學加壓效應，對此穿隧磁電阻材料於晶體結構、價數、磁性與電性之影響，以尋求最佳之磁電阻材料，期能應用於磁紀錄媒體上。此外本研究第二部分乃合成 $LiVMoO_6$ 鋰電池材料，並瞭解影響其電化學特性之因素。

關鍵詞：穿隧式磁電阻、雙層鈣鈦礦、$LiVMoO_6$

一、Abstract

Following the technological improvement, the information industry is changing day by day and various several media are keeping researching to satisfy the request of data storage and recording. Since 1995 materials of the TMR (tunneling magnetoresistance) effect were improved evidently, in a few years it's magnetic induction was doubled. TMR materials show much higher MR% (about 25~50%) than traditional GMR materials (about 10%) at room temperature, so it is considered be applied as the MR sensor in the magnetic recording industry. Accordingly, the first part of this research employs the chemical replacement that the Sr^{2+} with a bigger ionic radius is replaced by the smaller Ca^{2+} to synthesize a series of the TMR materials composed of $(Sr_{2-x}Ca_x)FeMoO_6$ $(0 \le x \le 2.0)$, to observe the influence of the chemical pressure effect on TMR materials in their crystal structure, valence, magnetic and electrical properties, which we discussed in this thesis in order to find the best TMR materials for the application in recording media. In the second part of this study, the $LiVMoO_6$ materials have been synthesized. Moreover, their electrical properties have been discussed.

Keywords: tunneling magnetoresistance (TMR)、double perovskites、$LiVMoO_6$

二、緣由與目的

Half-metallic compounds which have electrons with only one spin direction at the Fermi level have recently received considerable attention for their potential applications in spintronics.[1] Several magnetic oxides have been identified as having half-metallic behavior at low temperatures, however, their spin polarization is strongly reduced at room temperature (RT).[2] Therefore, oxides with both high spin polarization and high Curie temperatures are of particular interest. Recently, Kobayashi et al.[3] have reported a high spin polarization for an oxide material with a double-perovskite structure, Sr_2FeMoO_6 which also has a high Curie temperature, (Tc = 420 K).

In Sr_2FeMoO_6, the Fe^{2+} or Fe^{3+} ions are in a high-spin state with all the spin-up 3*d* orbitals occupied. Sleight and Weiher[4] proposed that if the spin-down 3*d* orbitals of Fe have similar energy to the 4*d* orbitals of Mo, the empty spin-down states (π^*-β) of Fe^{3+} are degenerate to the one electron occupied spin down states (π^*-β) of Mo^{5+} which may lead to the formation of a narrow band. The electrons in this band have antiparallel spins to the localized spins in the spin-up states (σ^*-α and π^*-α) of Fe^{3+}. A ferromagnetic half-metallic state is thus observed in this ordered perovskite with localized up-spins of Fe^{3+} and itinerant spin-down electron of Mo^{5+}. This is supported by the band calculations, which show at the Fermi level a mixing of the spin-down O 2*p*, Fe 3*d* and Mo 4*d* bands.[3,5-6] This band description is equivalent to an internal redox equilibrium between (Fe^{2+} + Mo^{6+}) and (Fe^{3+} + Mo^{5+}) states.

Further studies on other members of the $A_2BB'O_6$ (where A = alkaline-earth or rare-earth ion, B and B′ = transition metal ion) family of double perovskites show that the occurrence of magnetoresistance (MR) properties is a fairly common feature. The A = Ca and Ba analogues of A_2FeMoO_6 were also found to display half-metallic and ferrimagnetic properties.[7-10] Moreover, the A_2FeReO_6 (A = Ca, Sr, Ba) compounds

exhibit[11-12] a half-metallic ground state concomitant with ferrimagnetic coupling of Fe^{3+} and Re^{5+} ($5d^2$, S = 1) magnetic moments, and show MR at RT. It is thus of great interesting to explore other prospective half-metallic compounds with large MR effects at low magnetic fields, in ferromagnetic compounds with *T*c as close to RT as possible. Studies of polycrystalline samples,[3,5-6,9,13] epitaxial thin films[14-15] and artificial grain boundaries,[16] have demonstrated that the negatively-spin-polarized conduction is the origin of the extrinsic, strong MR associated with spin-polarized tunneling between adjacent grains. This is known as tunneling magnetoresistance (TMR). Better understanding of the factors that control the structural, magnetic and conduction properties of these compounds is critical to optimize their properties for the applications based on their TMR effects.

In the recent report, Goodenough et al.[17] have first report on the series samples of $S_{r2-x}Ca_xFeMoO_6$ $0 \leq x \leq 2$. They found that ferromagnetic long-range ordered domains are coupled antiferromagnetically across antiphase boundaries; random disorder within domains may be small. In this article we aim to investigate in detail the variation of crystal structure and magnetic properties of the $(Sr_{2-x}Ca_x)FeMoO_6$ ($0 \leq x \leq 2.0$) double perovskite system due to chemical substitution of the smaller Ca^{2+} ions for the bigger Sr^{2+} cations, which applies an internal chemical pressure. We report systematic structural phase changes from tetragonal to monoclinic symmetry and a decrease in the refined Fe/Mo anti-site disorder at $x \geq 1.5$. Most interestingly, we demonstrate the dramatic changes in the magnetic and transport properties upon tuning the Ca doping amount in the Sr site, which enhances the TMR properties described previously for Sr_2FeMoO_6.

In other hand, mixed transition metal oxide $LiVMoO_6$ was synthesized by solid-state reaction method and was exploited as an anode material for use in rechargeable lithium-ion batteries. The electrochemical characteristics of the prepared electrodes assembled in coin cells were investigated in terms of half-cell performance. It was observed that the cell exhibits three discharge plateaus. The total discharge capacity, averaged over several test runs, is about 1250 mAh/g. The mechanism of electrochemical reaction of $LiVMoO_6$ with Li was studied *in-situ* by synchrotron XRD method. It was found that $LiVMoO_6$ undergoes irreversible decomposition during the first discharge.

三、研究方法

Sample Preparation. The samples of $(Sr_{2-x}Ca_x)FeMoO_6$ ($0 \leq x \leq 2.0$) were prepared by the solid state reaction method. Stoichiometric mixtures of high purity oxides $SrCO_3$, $CaCO_3$, Fe_2O_3, and MoO_3 were first calcined in air at 800 °C for 12 h. The obtained powders was ground and pressed into pellets (15 mm in diameter and 3 mm in thickness). The pellets of $(Sr_{2-x}Ca_x)FeMoO_6$ ($0 \leq x \leq 1.5$) were sintered at 1000 °C for 38 h in a 5 % H_2 / N_2 gas mixture, and the pellet with x = 2.0 was sintered at 1200 °C for 12 h in a 5 % H_2 / N_2 gas mixture.

The $LiVMoO_6$ was synthesized via solid-state reaction of Li_2CO_3, V_2O_5 and MoO_3. Well ground mixture of starting materials was sintered at 550°C in air for 24 h.

Characterization. X-ray diffraction (XRD) measurements were carried out on a SCINTAG (X1) diffractmeter (Cu Kα radiation, λ = 1.5406 Å) at 40 kV and 30 mA. The GSAS program was used for the Rietveld refinements in order to obtain information on the crystal structures of $(Sr_{2-x}Ca_x)FeMoO_6$. A pseudo-Voigt function was chosen to generate the line shape of the diffraction peaks. In the final runs, the positional coordinates, isotropic thermal factors, and anti-site disorder of Mo and Fe atoms were refined. Scanning electron micrographs (SEMs) were measured at room temperature by a Philips XL30 SEM equipped with a field emission gun at 15 kV. Electron diffraction (ED) and high resolution transmission electron microscopy (HRTEM) were carried out using a JEOL 4000EX electron microscope operated at 400 kV. Image simulation was made using CaRIne software. The samples for microscopic measurement were dispersed in alcohol before being transferred to the carbon coated copper grids. The resistively measurements at zero field [($\rho(T)$)] and under a magnetic field [($\rho(H)$)] were performed with a Quantum Design PPMS (physical properties measurements system), using the conventional four probe technique, under magnetic fields up to 3 T. Magnetization measurements were performed on a SQUID magnetometer from 0 to 350 K.

X-ray absorption near edge structure (XANES) measurements at Fe-L_{23} and Mo-M_{23} edges were performed at the synchrotron radiation research center (SRRC) in Hsinchu, Taiwan with an electron beam energy of 1.5 GeV and a maximum stored current of 240 mA. The spectra were recorded by measuring the sample current. The incident photon flux (I_0) was monitored simultaneously by using a Ni mesh located after the exit slit of the monochromatic beam. All the measurements were performed at room temperature. The reproducibility of the adsorption spectra of the same sample in different experimental runs was found to be extremely good.

In-situ XRD measurements were carried out at beamline BL17A1 of National Synchrotron Radiation Research Center (NSRRC) in Taiwan. The wavelength of the monochromatic X-ray was 1.3271 Å. In-situ synchrotron XRD experiments were carried out using coin cells with windows made from polyimide film. Aluminum current collector for anode was substituted by copper one to avoid strong synchrotron X-ray absorption by the copper metal. The electrochemical cell was discharged to 0.01 V at

a constant current of 0.3 mA and it took 13 min for recording each XRD pattern.

三、結果與討論

The powder XRD patterns of the $(Sr_{2-x}Ca_x)FeMoO_6$ ($0 \le x \le 2.0$) samples are shown in Figure1. Each composition of the series is single phase. For the samples with $x < 1.0$ and $x > 1.5$, all the peaks in each pattern can be indexed on the basis of a tetragonal unit cell (space group: *I*4/*m*) and monoclinic (space group: $P2_1/n$), respectively. This indicates that in the x = 1-1.5 region the structure changes from tetragonal to monoclinic at RT. The initial structural models fitted with the Rietveld profile method were based on Sr_2FeMoO_6 for x = 0, 0.5 and 1.0 and Ca_2FeMoO_6 for x =1.5 and 2.0. Figures 2 (a) and (b) display the observed and calculated X-ray powder diffraction profiles at 300 K of $(Sr_{2-x}Ca_x)FeMoO_6$ with x = 0.5 and 2.0. All the observed peaks can be fitted with the reflection conditions of the space groups *I*4/*m* for x = 0.5 and $P2_1/n$ for x = 2.0, respectively. Free refinement of the atomic positions was possible for all samples except those on either side of the structural transition (x = 1.0 and 1.5). For these materials, the coordinates were fixed, at the x =0.5 values for the x =1.0 refinement, and at the x = 2.0 values for the x = 1.5 refinement. In the final refinements, the possibility of anti-site disordering due to some Mo sites being occupied by Fe atoms and vice versa was taken into account. The refined occupancies of the Fe and Mo show that the Fe/Mo anti-site disorder is abruptly decreased in x = 2.0 of $(Sr_{2-x}Ca_x)FeMoO_6$. Recently, Alonso et al. proposed that the actual degree of order depends mainly on the synthesis conditions. Therefore, an increase in order of the x = 2.0 sample may be due to the higher synthesis temperature (1200 ℃). The lattice parameters (*a* and *c*) and cell volume (inset of Figure 3) decrease with increasing Ca content as noted in Figure 3, due to the substitution of the smaller Ca^{2+} ions (1.34 Å) for the larger Sr^{2+} (1.44 Å) cations. Importantly, these structural parameters indicate that the structure phase transition is continuous.

The morphology and particle size of the $(Sr_{2-x}Ca_x)FeMoO_6$ ($0 \le x \le 2.0$) samples probed by SEM are shown in Figure 4. An increase of particle size with increasing Ca content (from ~1 μm at x = 0 to ~2 μm at x = 2.0) was observed. This indicates that the incorporation of Ca into Sr sites facilitates grain growth during the sintering process.

Figures 5 (a) and 5 (b) show a typical ED pattern and HRTEM lattice image, respectively, recorded along the [001] zone-axis direction of Sr_2FeMoO_6. The simulated pattern along zone axis [001] is shown in Figure 5 (c). The cell symmetry obtained by ED was identified by the observation only of *h k l; h + k + l = 2 n* reflections indicating *I*-centering of the unit cell which is consistent with the XRD refinement result. Moreover, the HRTEM lattice image shows a tetragonal cell with $a = b \sim 5.57$ Å. In Figures 6 (a) and 6 (b) are the typical ED pattern and the HRTEM lattice image recorded along the [111] zone-axis direction of Ca_2FeMoO_6. The simulated pattern along the [111] zone axis is shown in Figure 6 (c). The agreement between experimental and calculated [111] HRTEM images confirms the correctness of the structural model.

Figure 7 shows the temperature dependence of high-field (H = 5 T) magnetizations of $(Sr_{2-x}Ca_x)FeMoO_6$ ($0 \le x \le 2.0$) samples. The substitution of Sr^{2+} by Ca^{2+} systematically increases the ferromagnetism, although the magnetizations of the x = 1.0 sample is anomalously low and is below that of the x = 0.5 sample. The magnetization isotherms of $(Sr_{2-x}Ca_x)FeMoO_6$ are typically ferromagnetic with negligible remanence and coercivity as illustrated in Figure 8. The saturation magnetizations at 5 K for all the studied compounds are listed in Table 2. For the $x \ge 1.5$ samples, the obtained values are consistent with a ferromagnetic state near the expected 4 μ_B fu^{-1} for a nominal ionic configuration Fe^{3+} (S=5/2) / Mo^{5+} (S=1 2). However, in $x < 1.5$ samples, the observed total magnetic moment is smaller than the expected value. This variation can be attributed to the effect of anti-site disorder at the octahedral Fe, Mo cation sublattices. The anti-site cation occupancy, p, ideally reduces the net moment to 4-2p μ_B fu^{-1}, however, the local magnetic disorder caused by the anti-site defects reduces the ordered moment still further.

The transport properties of $(Sr_{2-x}Ca_x)FeMoO_6$ (x = 0.5, 1.0, and 2.0) are illustrated in Figure 9 (a). Both ρ(H = 0) and ρ(H = 3T) show a semi-metallic behavior over the whole temperature range, down to 5 K. The observed value for x = 2.0, ρ (T = 300 K, H = 0), of 2×10^{-3} Ω cm is considerably smaller than that of the Sr doped analogues (x = 0.5 and 1.0).

The magnetotransport properties are shown as the evolution of MR (3 T), defined as: MR (T,H) = [ρ (T,H = 0) − ρ (T,H = 3 T)]/ ρ (T,H = 3 T), in Figure 9 (b). The highest MR ratio appears in the x = 2.0 sample which has a low Fe/Mo anti-site disorder and the highest magnetization. However, the x = 2.0 sample has a mush lower *T*c (*T*c~377 K) [8] which makes it less interesting than that of the x = 0 sample (*T*c = 420 K).[3] Lower MR ratios are found in the $x \le$ 1.0 samples which have a higher Fe/Mo disorder and lower magnetizations. The anti-site chemical substitution is known to lower the MR ratio in Sr_2FeMoO_6 samples.

The Fe L-edge XANES spectra of $(Sr_{2-x}Ca_x)FeMoO_6$ (x = 0 , 0.5 , 1.0 and 1.5) are shown in Figure 10 (a). For comparison, the spectra of FeO, Fe_2O_3 and Fe_2O_3 are also plotted. The spectra show two broad multiplet structures separated by spin–orbit splitting (of Fe $2p_{3/2}$ and $2p_{1/2}$). The chemical shift does not vary significantly although the Fe profile changes systematically when the Ca content is increased from x = 0 to x =1.5. It is well established that an effective Fe valence can be

measured from the peak width at the Fe 2*p* X-ray adsorption edge in FeO and Fe_2O_3. We therefore adopted the same scheme to obtain the Fe valence. As deduced from Figure 10 (a), the Fe valence is much greater than 2+ but less than 3+ over the range of Ca substitution. Here, the relative intensity ratio of the energy at 710 eV and 708 eV [as denoted by I(710)/I(708)] corresponding to the ratio of $Fe^{3+}$and Fe^{2+} increases with x is shown in the inset of Figure 10(a). The average valence for Fe has also been found to be intermediate between high-spin configurations values of Fe^{2+} and Fe^{3+} from MÖssbauer spectroscopy studies. From the chemical formula $(Sr_{2-x}Ca_x)FeMoO_6$, assuming oxygen stoichiometry, if the valence of Fe is 2+y, then Mo should formally be in the 6-y state. In Figure 10 (b), the Mo M-edge absorption spectra of $(Sr_{2-x}Ca_x)FeMoO_6$ along with those of MoO_2 (Mo^{4+}), and MoO_3 (Mo^{6+}) standards are shown. The intense peaks at the Mo M-edge onset involve 3*p*-core to 4*d* final-state transitions. These features can provide a probe of the 4*d* states, albeit modified by transition matrix element, core-hole-interaction and multiplet effects. Two strong spectral features are clearly visible in the MoO_3 standard: the low energy peak (A), due to the 3*p* to 4*d* t_{2g} excitations; and the high-energy peak (B), due to 3*p* to 4d_{eg} excitations. A clear decrease in the relative (B)-feature strength strongly supports the Mo-valence reduction with the increasing Ca-content which is shown in the inset of Figure 10 (b). The relative intensity ratio of the energy of 400.6 eV and 398.7 eV [as denoted by I(400.6)/I(398.7)] corresponding to the ratio of Mo^{6+} and Mo^{4+} decreases with an increase in x. Moreover, the Mo valence is consistent with a significant value of y<1 in the formal value of 6-y.

Figure. 11a shows the electrochemical properties of the $LiVMoO_6$ anode at room temperature. The cell was cycled between 4.25 and 2.80V. Although the ratio of the discharge capacity to charge in each cycle remains almost 95% for 30 cycles, the absolute values of the capacities were very low (0.12 mAh/g).

Besides the above range, coin type cells were also cycled at the discharging/charging current of 0.3 mA between 3.00 and 0.01 V (Fig. 11b). For the discharge course of the first cycle, the potential rapidly drops to reach a plateau, and then continuously decreases down to 0.01 V. The amplitudes of three plateaus are about 2.1-2.0 V, 0.6-0.5 V and 0.2-0.01 V, respectively. The total discharge capacity, averaged over several test runs, is about 1250 mAh/g. This value is much higher than the capacities exhibited by many conventional and newly discovered anode materials (graphitic carbons, tin-based amorphous oxides, amorphous vanadates have capacities of 370 – 800 mAh/g). Concerning the huge discharge capacity of $LiVMoO_6$, one could expect that if a low voltage reaction of the oxide were to occur, it would be even a total displacement reaction to form elemental V and Mo. Recently, the mechanism of lithium insertion into many binary and mixed oxides as well as their reactivity towards lithium [e.g. CoO, RVO_4 (R = In, Ce, Fe, Al and Y), $M_3B_2O_6$ (M = Co, Ni and Cu), $LiFePO_4$ etc.] were reported. Li insertion into some of these compounds is accompanied by their irreversible transformation into amorphous materials with formation of nanosized metal particles dispersed into the Li_2O matrix. Electrolyte degradation and growth of electrochemically active polymer-type coating over metal oxide particles increase the material capacity beyond theoretical values predicted for the complete reduction of transition metal oxide to pure metal.

The reversible capacity of $LiVMoO_6$ for the first cycle was only about 450 mAh/g reavealed that only one third of Li ions intercalated (or deposited) into this layered material can be extracted out. Furthermore, there was no distinct charge or discharge plateau observed in the subsequent cycles. The different profiles between the first and the following cycles implied that the electrochemical behaviors of the anode electrode were changed. This phenomenon implies that an irreversible phase transformation of $LiVMoO_6$ occurred after it reacted with lithium ions in a non-aqueous phase. Consequently, we suggest that it is required to be "activated" by over-doping with lithium ions *via* the electrochemical reaction before the first use. From the second cycle the reversible capacity decayed continuously until the fortieth cycle. After the fortieth to hundredth cycle, the coulombic charge/discharge efficiency of each cycle remains > 95%.

In order to elucidate the structural transformation occurring upon cycling, in-situ XRD measurements were carried out. In Figure 12, XRD patterns taken during the course of first discharge (see inset of Fig. 12) are shown. Inset shows the points on the discharge curve at which the XRD measurements were performed. The XRD pattern in Fig. 12a shows the diffraction peaks corresponding to $LiVMoO_6$ structure along with some additional signals related to the aluminum foil substrate. The unavoidable reason of using the Al foil as a current collector instead of the Cu one is related to a higher X-ray absorption coefficient at the wavelength of 1.3271 Å for the latter. As we know, Li can alloy with Al under electrochemical conditions at low voltages. Thus this would result in mis-interpretation of the capacities and voltages observed in the measurement. Fortunately, the discharge profile of the $LiVMoO_6$ electrode coated on an Al foil (inset of Fig. 12) was very similar to that of the electrode using Cu foil (Fig. 11b). In addition, their total discharge capacities were almost the same. Several studies on the corrosion behavior of aluminum current collectors in lithium ion batteries indicated that thermodynamically Al is expected to corrode during charging/discharging process as the standard electrode potential of aluminum (1.39 V vs. Li/Li^+) is much lower than the normal operating potential of the positive electrode. However, the self-discharge rate of the lithium ions on the Al substrate is very low. Moreover, aluminum

is always kinetically stable in many circumstances because it is readily covered with a passive film. As a result, the observed corrosion resistance of the aluminum could be due to its native thin oxide layer. The transformation of the original $LiVMoO_6$ phase to assumed Li_xVO_2 ($x \leq 1$) phase (as indicated by * in Fig. 12) is progressively increasing during discharge. In this case molybdem oxide can form amorphous phases. In other words, these growing peaks were not derived from the primitive patent, implying that the mechanism of the electrochemical reactions is not simply the conventional intercalation-deintercalation processes during the first discharge. This reasoning seems plausible because the space between the adjacent lattice layers is not large enough to accommodate up to about 8-10 Li atoms per formula unit of $LiVMoO_6$. The lithium ions moving from the Li foil electrode through the electrolyte also did not aggregate and be reduced to form any metallic deposition, for instance, the lithium metal dendrite, in the $LiVMoO_6$ electrode. On the whole, we wish to emphasize that the cycle ability of the $LiVMoO_6$ electrode may be induced by some uncertain species produced by the reaction of Li ions with $LiVMoO_6$.

We examine further about the importance of the electrochemical activation process that we have been considering. The surface morphology of the $LiVMoO_6$ anode before and after cycling examined by SEM is shown in Figure 13. The particle size distribution of $LiVMoO_6$ before discharge is broad; the estimated grain size varies from 1 to 10 μm. As seen from the micrograph in Figure 13a, almost all the particles have clear and linear grain boundaries and also a pore-free surface after sintering at 550°C. It is also interesting to note that the clear grain boundaries became blurred after discharge, as shown in Figure 13b, and some translucent materials were observed on the surface of the particles. The results of in-situ XRD measurement shows clear evidence for this observation. The intensities and shape of diffraction peaks of $LiVMoO_6$ become lower and broader gradually during the discharge process. These phenomena seems to indicate that the well-crystallized $LiVMoO_6$ powder decomposes to nano-scale particles or even to amorphous phases, and the organic electrolyte molecules were also deposited on the surface of $LiVMoO_6$ *via* some electrocatalytic reactions. Although the $LiVMoO_6$ material cannot retain its crystallinity after discharge, the new phase, i.e. the products of decomposed $LiVMoO_6$, still show significant reversibility of cycling. The assumption that the nano-sized materials can exhibit quite different properties from bulk materials is now widely accepted. Therefore, the electrochemically driven size confinement of the decomposed particles is believed to be a key factor in enhancing their electrochemical activity towards lithium metal.

五、結論

The increasing Ca-content in $(Sr_{2-x}Ca_x)FeMoO_6$ samples increases the magnetic moment close to the theoretical value due to a reduction of Fe/Mo anti-site disorder. An increase of conductivity with Ca-doping is also observed resulting from an increase in the Fe $3d-$Mo $4d$ band overlap. This is explained from simple ionic size arguments and is supported by XANES spectra and band structure calculations. We conclude that the chemical pressure effects of doping Ca from Sr site is an important factor in control the charge transfer and hence the electrical and magnetic properties of the magnetoresistive Sr_2FeMoO_6 type materials.

$LiVMoO_6$ was successfully synthesized using the conventional solid-state reaction method. It was shown that $LiVMoO_6$ may be considered as an anode material of choice for rechargeable lithium-ion batteries. *In-situ* synchrotron XRD experiments were performed to elucidate the phase transformations in $LiVMoO_6$ anode during its first discharge. It was shown that electrochemical cycling of $LiVMoO_6$ anode goes through decomposition of the pristine compound and results in the formation of nano-scale amorphous particles.

六、計畫成果自評

We have reached the goals of the research plan, some part of the results have already publicized in scientific journals [18-37].

七、參考文獻

(1) Prinz , G. *Science*. **1998**, *282***,** 1660.
(2) Gupta, A.; Sun, J. Z. *J. Magn. Magn. Mater*. **1999**, *200*, 24.
(3) Kobayashi, K. -I.; Kimura, T.; Sawada, H,; Terakura, K.; Tokura, Y. *Nature*. **1998**, *395*, 677.
(4) Sleight, A. W.; Weiher, J. F. *J. Phys. Chem. Solids*. **1972**, *33*, 679.
(5) Kim, T. H.; Uehara, M.; Cheong, S. W.; Lee, S. *Appl. Phys. Lett*. **1999**, *74*, 1737.
(6) Fang, Z.; Terakura, K.; Kanamoru, J. *Phys. Rev. B* **2001**, *63*, 180407.
(7) Maignan, A.; Raveau, B.; Martin, C.; Hervieu, M. *J. Solid State Chem*. **1999**, *59*, 11159
(8) Alonso, J. A.; Casais, M. T.; Martínze-Lope, M. J.; Velasco, P.; Muñoz, A.; Fernández-Díaz, M. T. *Chem. Mater*. **2000**, *12*, 161.
(9) Borges, R. P.; Thomas, R. M.; Cullinan, C.; Coey, J. M. D.; Suryanarayan, R.; Ben-Dor, L.; Pinsard-Gaudart, L.; Revcolevschi, A. *J. Phys. Condens. Matte*r. **1999**, *11*, L445.
(10) Ritter, C.; Ibarra, M. R.; Morellón, L.; Blasco, J.; García, J.; De Teresa, J. M. *J. Phys.: Condens. Matte*r. **2000**, *12*, 8295.
(11) Prellier, W.; Smolyaninova, W.; Bisbas, A.; Galley, C.; Greene, R. L.; Ramesha, K.; Gopalakrishnan. J. *J. Phys. Condens. Matter*. **2000**, *12*, 965.

(12) Kobayashi, K. -I.; Kimura, T.; Sawada, H,; Terakura, K.; Tokura, Y. *Phys. Rev. B* **1999**, *59*, 11159.

(13) García-Landa, B.; Ritter, C.; Ibarra, M. R.; Blasco, J.; Algarabel, P. A.; Mahendiran, R.; García, *J. Solid State Commun*. **1999**, *110*, 435.

(14) Lu, K. Q.; Stern, E. A. *Nucl. Instrum. Methods* **1983**, *212*, 475.

(15) Manako, T.; Izumi, M.; Konishi, Y.; Kobayashi, K. -I,; Kawasaki, M.; Tokura, Y. *Appl. Phys. Lett*. **1999**, *74***,** 2215..

(16) Yin, H. Q.; Zhou, J. S,; Zhou, J. P.; Dass, R.; McDevitt, J. T.; Goodenough, J. B. *Appl. Phys. Lett*. **1999**, *75*, 2812.

(17) Goodenough, J. B.; Dass, R. I. *Inter. J. Ino. Mater.* **2000**, *2*, 3.

(18) T. S. Chan, R. S. Liu, G. Y. Guo and C. Y. Huang, (2003), "Synthesis and Characterization of Double Perovskites Sr_2FeMoO_6 (M = Mo, W)", *Inter. J. Mod. Phys.* B, 17, 3500-3502.

(19) T. S. Chan, R. S. Liu, G. Y. Guo, S. F. Hu, J. G. Lin, J. -F. Lee, L. -Y. Jang, C. -R. Chang and C. Y. Huang, (2004), "Structural, Electrical and Magnetic Characterization of the Double Perovskites Sr_2CrMO_6 (M = Mo, W): B´ 4d-5d System", *Solid State Commu.*, 130, 815-820.

(20) R. S. Liu, H. M. Chen and S. F. Hu, (2004), "Synthesis and Characterization of Nano Metals with Core-Shell Structure", *China Particuology* 2, 160-163.

(21) S. F. Hu, R. L. Yeh and R. S. Liu, (2004), "Coulomb Blocakade Effect in Self-assembled Gold Quantum Dots", *China Particuology* 2, 174-176.

(22) R. S. Liu, S. C. Chang and J. M. Chen, (2004), "Role of Pb in High-T_c Bi-based Superconductors", *Chin. J. Phys.* 42, 549-554.

(23) S. W. Lin, S. C. Chang, R. S. Liu, S. F. Hu and N. T. Jan, (2004), "Fabrication and Magnetic Properities of Nickel Nanowires, *J. Mag. Mag. Mat.* 282, 28-31.

(24) T. S. Chan, R. S. Liu and C. Y. Huang, (2005), "Structural and Magnetic Properties of Double Perovskites Sr_2CrWO_6 ", *Int. J. Mod. Phys. B* 19, 537-540.

(25) R. S. Liu, T. S. Chan. S. Mylswamy, J. M. Chen and J. P. Attfield, (2005), "Charge Transfer in Half-metallic $(Sr_{2-x}Ca_x)FeMoO_6$ System", *Chinese J. Phys.* 43, 751-756.

(26) A. A. M. Prince, S. Mylswamy, C. Y. Wang, S. C. Chang, R. S. Liu, C. H. Lin, Y. K. Lin, C. H. Shen, S. M. Huang and J. F. Lee, (2004), Electrochemical and In Situ XANES Studies of a $LiNi_{0.8}Co_{0.17}Al_{0.03}O_2$ cathode Material", *Solid State Commu.*, 132, 273-277.

(27) A. A. M. Prince, S. Mylswamy, T. S. Chan, R. S. Liu, B. Hannoyer, M. Jean, C. H. Shen, S. M. Huang, J. F. Lee, G. X. Wang, (2004), "Investigation of Fe Valence in $LiFePO_4$ by Mössbauer and XANES Spectroscopic Techniques, *Solid State Commu.*, 132, 455-458.

(28) T. S. Chan, R. S. Liu, G. Y. Guo, S. F. Hu, J. G. Lin, J. M. Chen and C. -R. Chang, (2005), "Effect of B'-site Transition Metal on the Properties of Double Perovskite Sr_2FeMO_6 (M =Mo, W):B' 4d-5d System, *Solid State Commu.* 133, 265-270.

(29) C. H. Lin, C. H. Shen, A. A. M. Prince, S. M. Huang and R. S. Liu, (2005), "Electrochemical Studies on Mixtures of $LiNi_{0.8}Co_{0.17}Al_{0.03}O_2$ and $LiCoO_2$ Cathode Materials for Lithium Ion Batteries, *Solid State Commu.* 133, 687-690.

(30) J. M. Chen, S. C. Chang, R. S. Liu, J. M. Lee, M. Park and J. H. Choy, (2005), "Soft x-ray absorption spectroscopy of heterostructured high-T_c superconducting nanohybrid : $X\text{-}Bi_2Sr_2CaCu_2O_8$ (X= I, HgI_2, and $(Py\text{-}CH_3)_2HgI_4$)", *Phys. Rev. B* 71, 094501-1-4.

(31)Y. S. Lin, R. S. Liu and B. -M. Cheng, (2005), "Investigation of the Luminescent Properties of Tb^{3+} Substituted YAG:Ce,Gd Phosphors, *J. Electrochem. Soc.* 152, J41-J45.

(32) T. S. Chan, R. S. Liu and J.-F. Lee, "Local Structure of Double Perovskites Sr_2FeMO_6 (M = Mo, W) Studied by X-ray Absorption Spectroscopy", Chinese J. of Phys. 42, 779-783 (2005).

(33) T. S. Chan, R. S. Liu, Y. H. Lien, C. Y. Huang and J. G. Lin, (2005), "Crystal Structure, Magnetic and Electrical Properties of $(Tb_{1-x}Na_x)MnO_3$ (x = 0 and 0.15)", Chinese J. of Phys. 43, 757-762.

(34) L. S. Chi, R. S. Liu and B. J. Lee, (2005), "Synthesis of Y_2O_3:Eu,Bi Red Phosphors by Homogeneous Co-precipitation and Their Photoluminescence Behaviors", *J. Electrochem. Soc.* 152, J93-J98.

(35) T. S. Chan, R. S. Liu, S. F. Hu and J.G. Lin, (2005), "Structure and Physical Properties of Double Perovskites Compounds Sr_2FeMO_6 (M = Mo, W)", *Mat. Chem. Phys.* 93, 314-319.

(36) J. -W. G. Bos, J. P. Attfield, T. S. Chan and R. S. Liu, (2005), "Valence states in $(La_{1+x}Ca_{1-x})CoRuO_6$ double perovskites", *Phys.Rev. B.* 72, 014101.

(37) T. S. Chan, R. S. Liu and L.-Y. Jang, (2005), "Fe and Cr K-edges EXAFS Study of Double Perovskite $(Sr_{2-x}Ca_x)FeMoO_6$ ($0 \le x \le 2.0$) and Sr_2CrMO_6 (M = Mo, W) Systems", *J. Chinese Chem. Soc.* 52, 721-724.

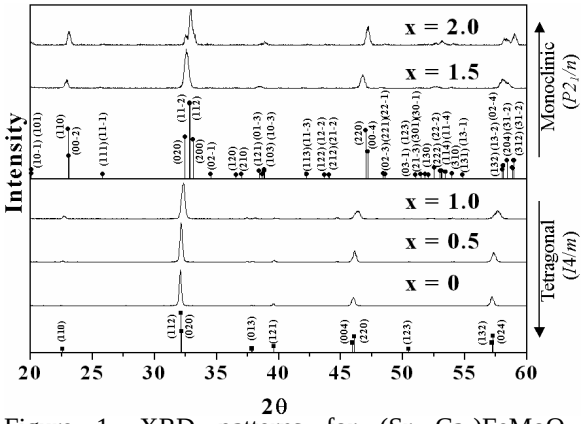

Figure 1. XRD patterns for $(Sr_{2-x}Ca_x)FeMoO_6$, indexed on a tetragonal unit cell (I4/m) for x = 0, 0.5 ,1, and indexed in a monoclinic unit cell ($P2_1/n$) for x = 1.5, 2.0.

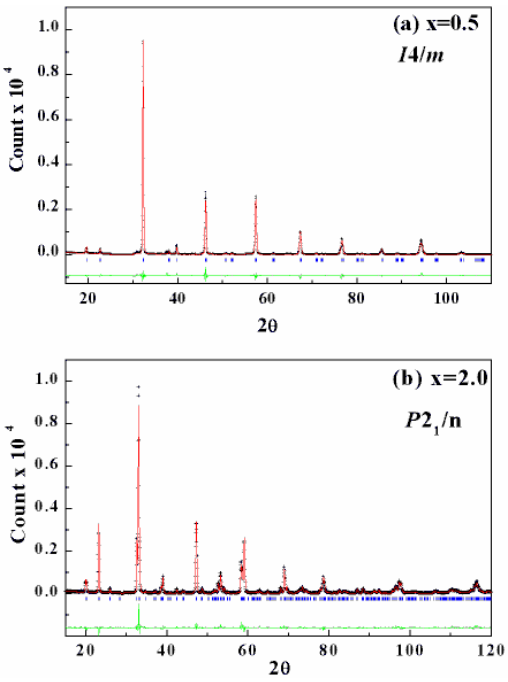

Figure 2. Rietveld fits to powder XRD data for $(Sr_{2-x}Ca_x)FeMoO_6$ with (a) x = 0.5; space group I4/m and (b) x = 2.0 space group $P2_1/n$, at 300K. Observed (crosses) and calculated (solid line) intensities are shown with the difference at the bottom.

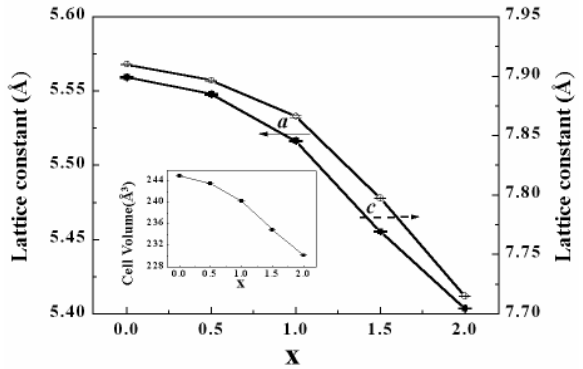

Figure 3. Lattice constants (a and c) as a function of x in $(Sr_{2-x}Ca_x)FeMoO_6$ ($0 \le x \le 2.0$). The cell volume as a function of x is shown in the inset.

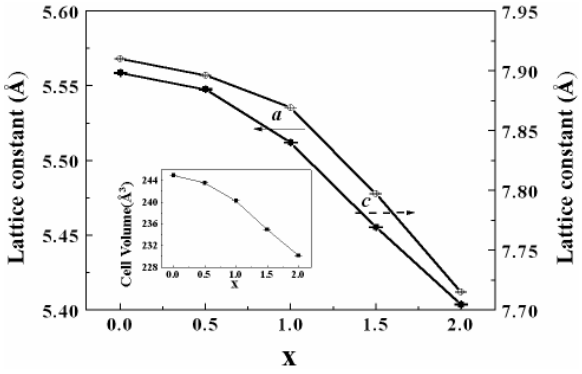

Figure 4. SEM photographs of $(Sr_{2-x}Ca_x)FeMoO_6$ ($0 \le x \le 2.0$)

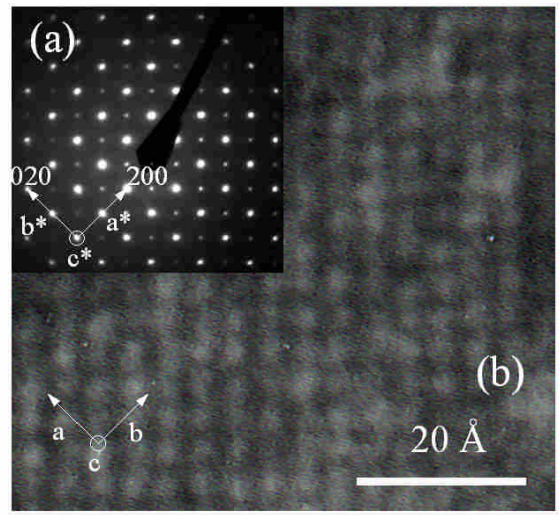

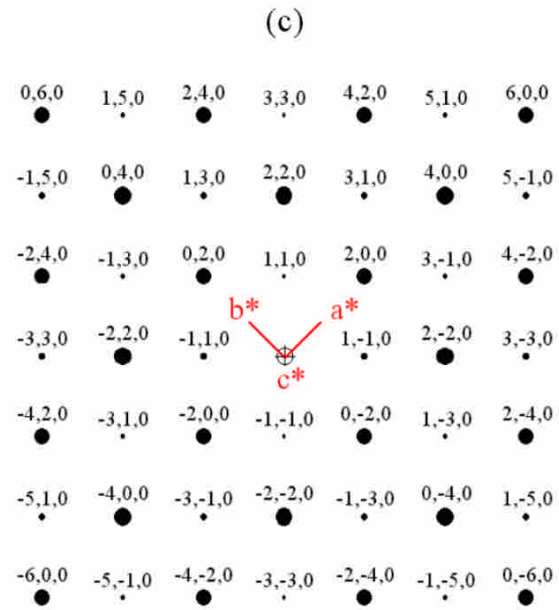

Figure 5.(a) ED pattern and (b) HRTEM lattice image along the [001] direction of $(Sr_{2-x}Ca_x)FeMoO_6$ (x = 0) sample. (c) Simulated pattern along the zone axis [001].

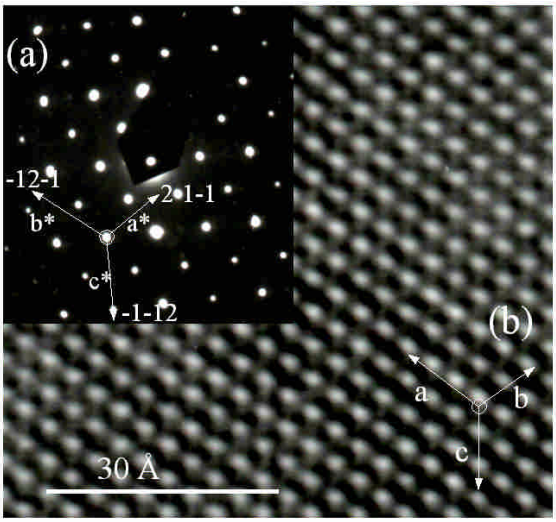

(c)

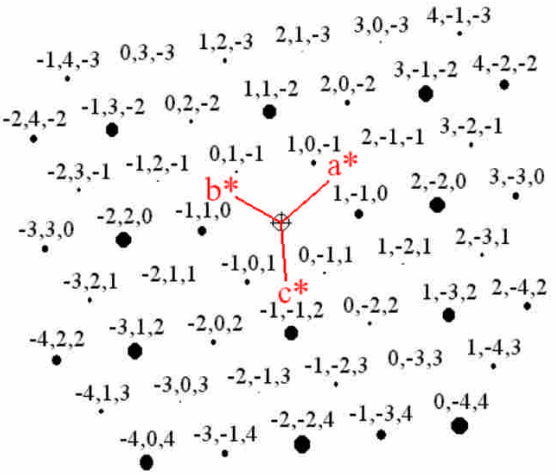

Figure 6. (a) ED pattern and (b) HRTEM lattice image along the [111] direction of $(Sr_{2-x}Ca_x)FeMoO_6$ (x = 2) sample. (c) Simulated pattern along the zone axis [111].

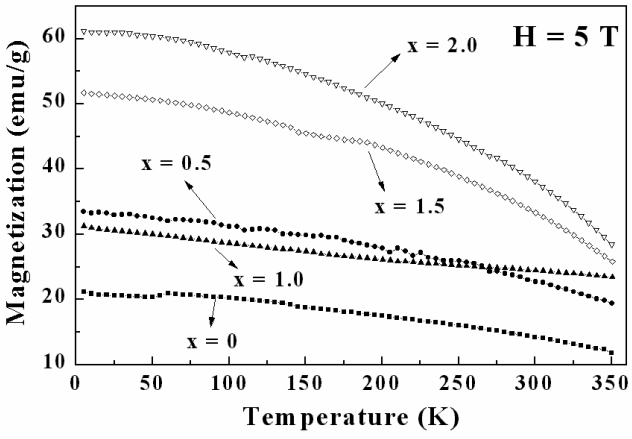

Figure 7. Temperature dependence of high-field (H = 5 T) magnetization of the $(Sr_{2-x}Ca_x)FeMoO_6$ ($0 \le x \le 2.0$).

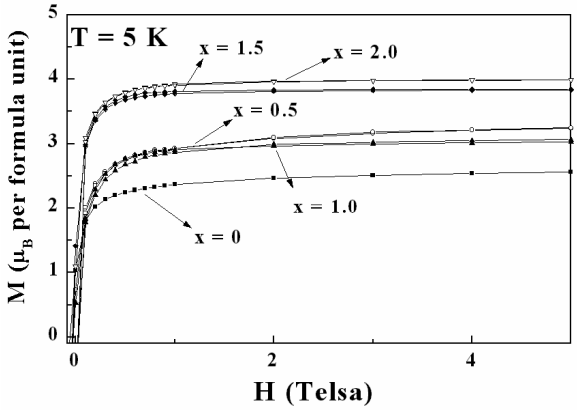

Figure 8. Magnetization isotherms of $(Sr_{2-x}Ca_x)FeMoO_6$ ($0 \le x \le 2.0$) at 5 K.

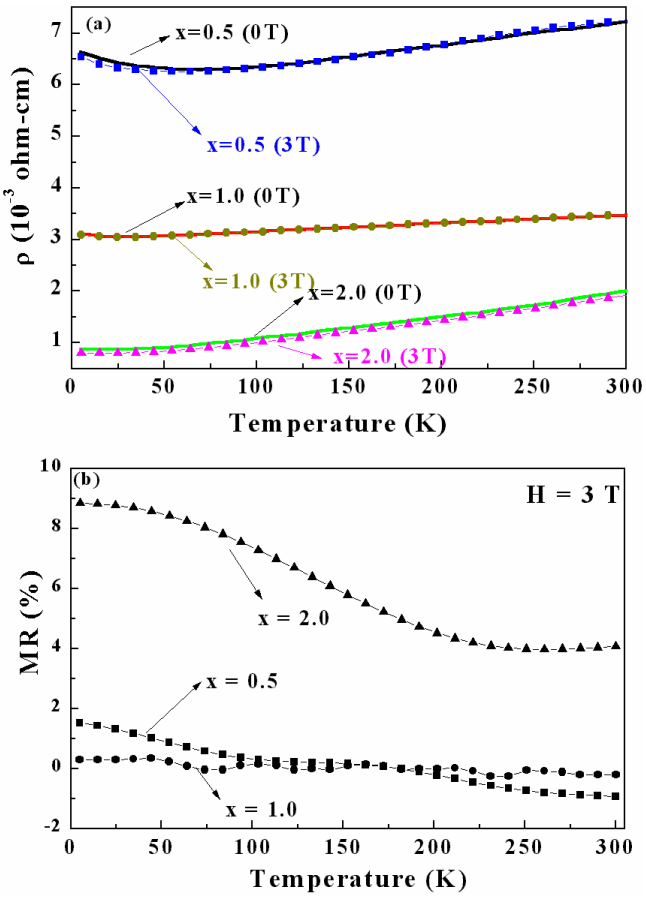

Figure 9. (a) Temperature dependence of resistivity of the $(Sr_{2-x}Ca_x)FeMoO_6$ (x = 0.5 and 1.0) samples. Effect of a magnetic field of 3 T is shown. (b) Plot of MR against temperature for $(Sr_{2-x}Ca_x)FeMoO_6$ (x = 0.5, 1.0, and 2.0).

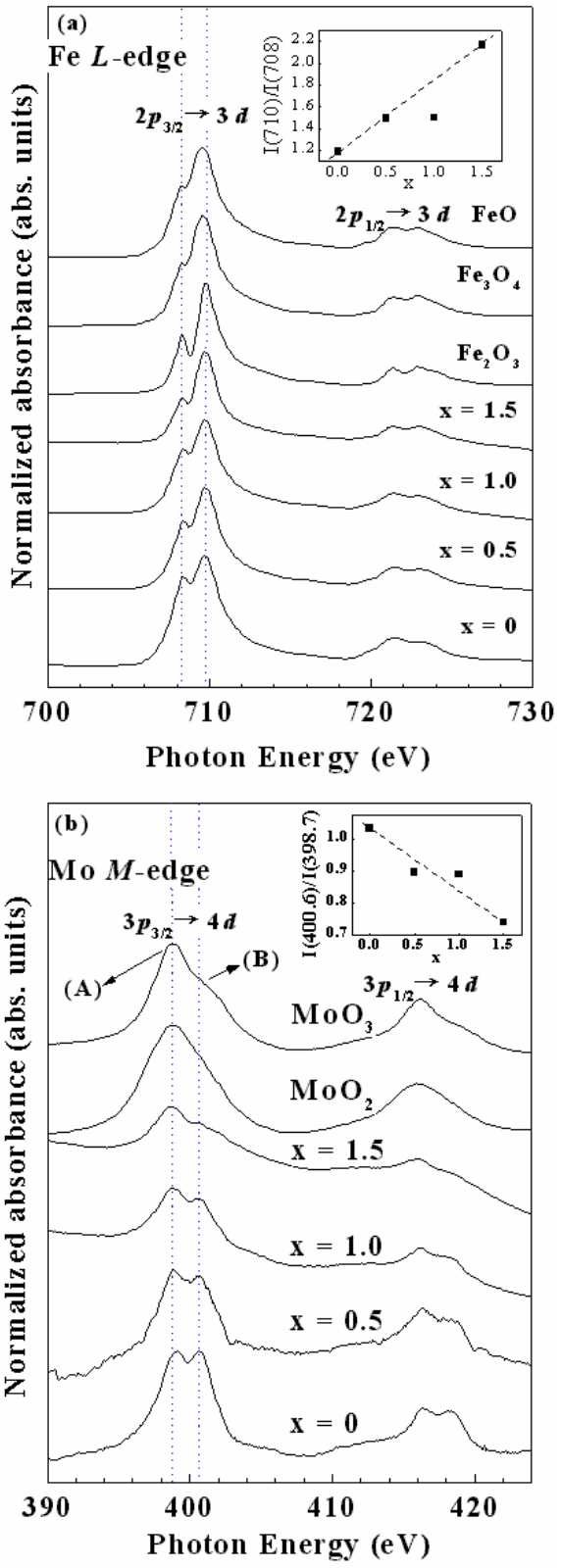

Figure 10. (a) Fe 2p-edge X-ray absorption near edge structure spectra of FeO (Fe^{2+}), Fe_2O_3 ($Fe^{2.67+}$), Fe_2O_3 (Fe^{3+}) and $(Sr_{2-x}Ca_x)FeMoO_6$ (x = 0 , 0.5 , 1.0 and 1.5). (b) Mo 3p-edge X-ray absorption near edge structure spectra of MoO_2 (Mo^{4+}), MoO_3 (Mo^{6+}) and $(Sr_{2-x}Ca_x)FeMoO_6$ (x = 0 , 0.5 , 1.0 and 1.5).

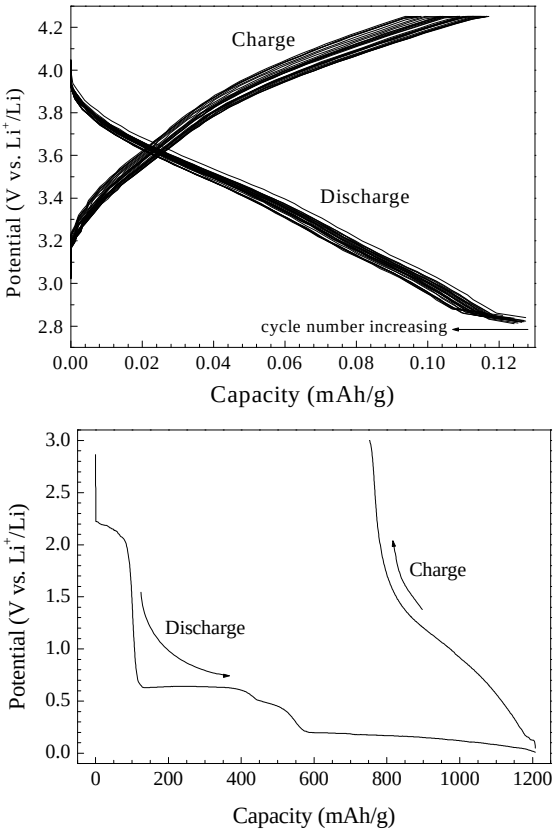

Figure. 11. Typical charge and discharge curves of $LiVMoO_6$ in the voltage range of 2.80-4.25 V (a) and 3.00-0.01 V (b).

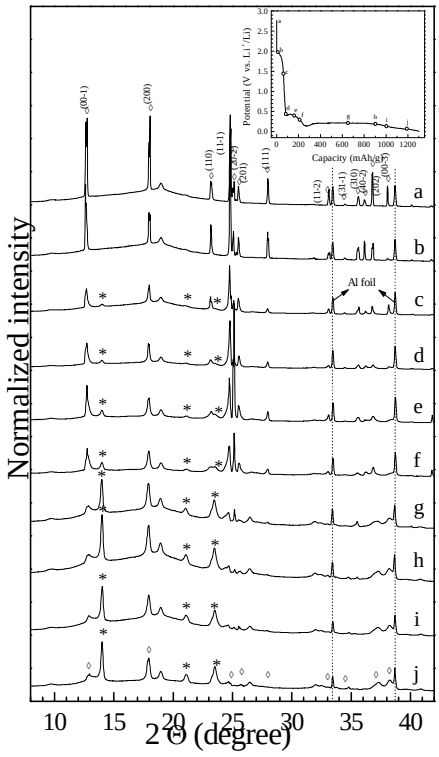

Figure. 12. In-situ X-ray diffraction patterns collected at various states of discharge of a $LiVMoO_6$/Li cell. Inset of this figure indicates the first discharge curve of the cell with Al current collector.

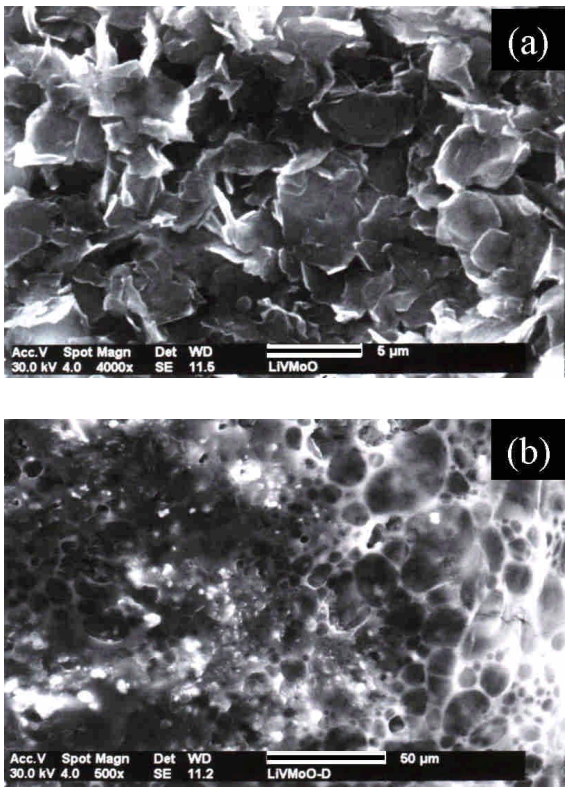

Figure. 13. SEM micrographs of the $LiVMoO_6$ electrode (a) before and (b) after cycling.